Supplemental Material:

Antipolar and short and long-range magnetic ordering in quasi-two-dimensional AgCrP$_2$S$_6$

Chaitanya B. Auti[1, *], Atul G. Chakkar[1], Shantanu Semwal [2], Sebastian Selter[3], Yuliia Shemerliuk[3], Bernd Büchner[3,4], Saicharan Aswartham[3], Koushik Pal[2], and Pradeep Kumar[1#]

[1]*School of Physical Sciences, Indian Institute of Technology, Mandi-175005, India.*

[2]*Department of Physics, Indian Institute of Technology Kanpur, Kanpur 208016, India*

[3]*Institute for Solid State Research, Leibniz IFW Dresden, Helmholtzstr. 20, 01069 Dresden, Germany*

[4]*Institute of Solid State and Materials Physics and Würzburg-Dresden Cluster of Excellence ct.qmat, Technische Universität Dresden, 01062 Dresden, Germany*

S1. Analysis of polarization dependent intensity:

The polarization-dependent measurements were performed by gradually rotating the incident light polarization using a half-wave plate (λ/2 plate) with increments of 20 degree, ranging from 0 to 180 degrees, while the polarization of the scattered light was fixed by using an analyzer. For convenience, we have mirrored the data points from 0 to 180 degrees.

The variation in intensity as a function of polar angle can be understood using a semi-classical approach. The Raman scattering intensity (I) is expressed as $I \alpha \left| \hat{e}_s^T . R . \hat{e}_i \right|^2$, where T is the transpose of the vector and R is the Raman tensor [1]. $\hat{e}_i$ and $\hat{e}_s$ represent unit vectors in the direction of incident and scattered light, respectively. For the above-mentioned configuration, incident and scattered light polarization unit vectors are given as $\hat{e}_i = \begin{bmatrix} \cos(\theta + \theta_0) & \sin(\theta + \theta_0) & 0 \end{bmatrix}$ and $\hat{e}_s = \begin{bmatrix} \cos(\theta_0) & \sin(\theta_0) & 0 \end{bmatrix}$, where θ is the relative angle between $\hat{e}_i$ and $\hat{e}_s$, whereas θ_0 is an arbitrary angle of scattered light from the X-axis when polarization unit vectors are projected in the XY-plane (*ab*-plane) as shown in the schematic, see Fig. S14. The Raman tensors for the phonon modes with A_g and B_g symmetries are listed in Table I. The angular dependence of the intensity of these modes is given as:

$$I_{A_g} = \left| b\cos(\theta+\theta_0)\cos\theta_0 + c\sin(\theta+\theta_0)\sin\theta_0 \right|^2, \qquad (1)$$

$$I_{B_g} = \left| f\sin(\theta+2\theta_0) \right|^2, \qquad (2)$$

without the loss of generality, θ_0 may be taken as zero, resulting in the expression (4) and (5) becomes:

$$I_{A_g} = |b|^2 \cos^2\theta, \qquad (3)$$

$$I_{B_g} = |f|^2 \sin^2\theta. \qquad (4)$$

The polarization dependence of the intensity of some phonon modes cannot be fitted using purely real tensor elements; therefore, a complex form of the Raman tensor should be used to describe the observed polarization dependence [2]. Here, the tensor element of A_g and B_g can be written as: $b = |b|e^{i\phi_b}$ and $c = |c|e^{i\phi_c}$, where ϕ_b and ϕ_c are the corresponding phases. Incorporating these complex elements, along with the polarization vectors $\hat{e}_i$ and $\hat{e}_s$, and the Raman tensor elements, into eqn (1) yields a modified equation of angular dependence intensities for A_g and B_g given as eqn (4) and (5) (see the main text).

S2. Temperature-dependent Photoluminescence:

Bulk AgCrP$_2$S$_6$ shows an indirect band gap, however, its flat band structure suggests that it may behave like a direct bandgap material. The photoluminescence (PL) spectra recorded using 532 nm laser displays a peak at $\sim$ 1.32/1.34 eV at temperature $\sim$ 6/300 K. Figure S16(a) represent the temperature evolution of the PL spectra in the temperature range of 6-300 K. The obtained spectrum shows an asymmetric lineshape; therefore, it is fitted using a bi-Gaussian function to extract the temperature-dependent energy (peak position), linewidth, and intensity. The asymmetry observed on the low-energy side of the PL spectrum may have many origins. At low temperatures, the occupation of lower energy states increases, potentially enhancing the contribution of dark excitons or recombination pathways involving localized

states, which can leads to asymmetry [3]. Additionally, preferential localization of cations within lattice may induces local dipole moments (stark effect), this can also contribute to asymmetry in PL spectra [4]. Figure S16(c-i) shows the temperature-dependent PL energy of $AgCrP_2S_6$ as extracted from our measurements. We observed a redshift up to ~ 40 K, possibly due to the lowering of the conduction band energy by the exchange interaction of the magnetic ions and conduction electrons [5]. Furthermore, at ~ 90 K a sharp change in slope is observed indicating anomaly at this temperature. A kink is observed at ~ 200 K, indicating another anomaly at ~ 200 K. Interestingly, temperature evolution of the PL spectra exhibits an unusual blueshift with increasing temperature, contrary to the typical behaviour observed in most semiconductors (see Fig. S16(b)). This anomalous temperature dependence cannot be accurately described using traditional empirical models like the Varshni [6], Pässler [7], and Bose-Einstein [8], which are commonly used for conventional semiconductors. This discrepancy likely arises from competing effects of electron-phonon renormalization and lattice thermal expansion on the band gap energy [9]. Similar type of behaviour is also reported for some perovskites [9,10]. From linear fitting, the energy obtained at 0 K is represented as $E_0 = 1.32$ eV. The continuous blue-shift in energy above temperature 90 K can be characterized by a temperature coefficient $\alpha = \partial E / \partial T = 0.071$ meVK^{-1}.

The temperature-dependent FWHM, denoted as $\Delta(T)$ and determined from the spectral lineshape, is plotted in Fig. S16(c-ii). It is observed that FWHM shows a kink ~ 40 K, after which it starts rapidly increasing from ~ 90 K. We use a linear exciton-phonon coupling model, commonly employed to analyse $\Delta(T)$, given as [11]:

$$\Delta(T) = \Delta_0 + \lambda_{AC}T + \lambda_{LO}N_{LO}(T),\qquad\qquad(5)$$

where the Δ_0 term accounts for linewidth broadening due to various factors such as impurities, dislocations, and imperfections. The second term of equation arises from exciton interactions

3

with acoustic phonons. The final term arises from exciton interactions with longitudinal optical (LO) phonon and is proportional to the Bose function, which represents the population of phonons at finite temperature and is given as: $N_{LO}(T) = 1/[e^{(E_{LO}/k_b T)} - 1]$; where E_{LO} is the energy of LO phonons and k_b is the Boltzmann constant. The coefficients λ_{AC} and λ_{LO} represent coupling strength of the exciton-acoustic/LO phonons, respectively. Exciton-LO phonon interactions are understood through the Fröhlich mechanism, while exciton-acoustic phonon interactions are described by the deformation potential. From the fitting eqn (5), the parameters obtained as follows: $\Delta_0 = 91.16 \pm 2.39$ meV, $\lambda_{AC} = 203.76 \pm 18.60$ µeVK^{-1}, $\lambda_{LO} = 3.98 \pm 2.46$ eV, $E_{LO} = 123.46 \pm 17.69$ meV. The exciton-acoustic phonon coupling strength is orders of magnitude smaller than the exciton-optical phonon coupling strength, indicating that optical phonons contribute significantly more to linewidth broadening than acoustic phonons. This is consistent with the observed large LO phonon energy. The temperature-dependent (PL) intensity, shown in Fig. S16(c-iii), decreases drastically from 6 K to 90 K. This intensity decrease is primarily attributed to thermal quenching. At low temperatures, the luminescence internal quantum efficiency is high because non-radiative recombination centres are minimized. As the temperature increases, these centres become thermally activated, capturing more photogenerated carriers. This, in turn, reduces the number of carriers available for radiative recombination, resulting in the observed decrease in the PL intensity [12]. Above ~ 200 K, the intensity then gradually increases with rising temperature, reason associated with this anomalous increase of intensity is unknown; however, we should stress that the anomalous temperature dependent PL of $AgCrP_2S_6$ demands further theoretical and experimental investigations.
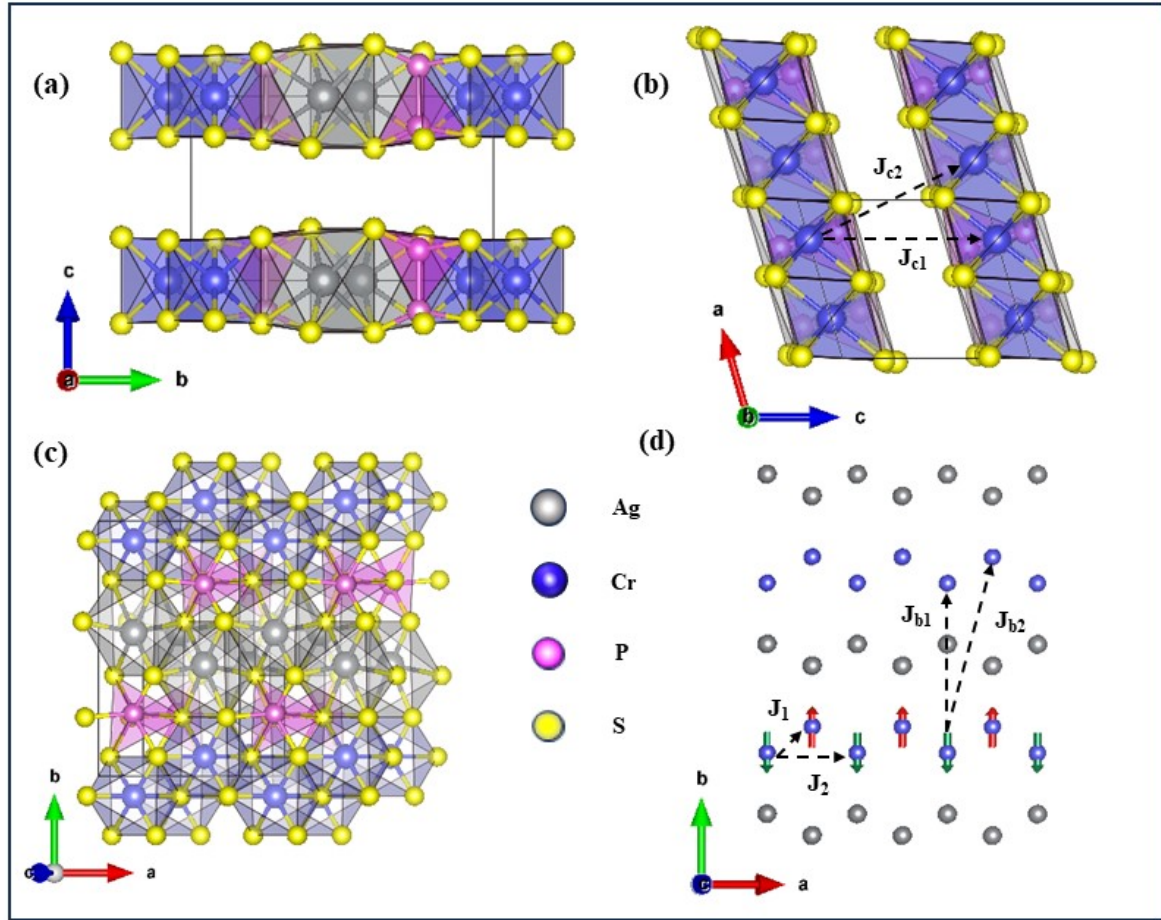
Figures:

Figure S1. (a)-(c) Shows the crystal structure of AgCrP$_2$S$_6$ in the *bc*, *ac*, and *ab* plane, respectively. (d) Zigzag chains of magnetic Cr^{3+} ions (spin up and down shown by arrows) and nonmagnetic Ag$^+$ ions.
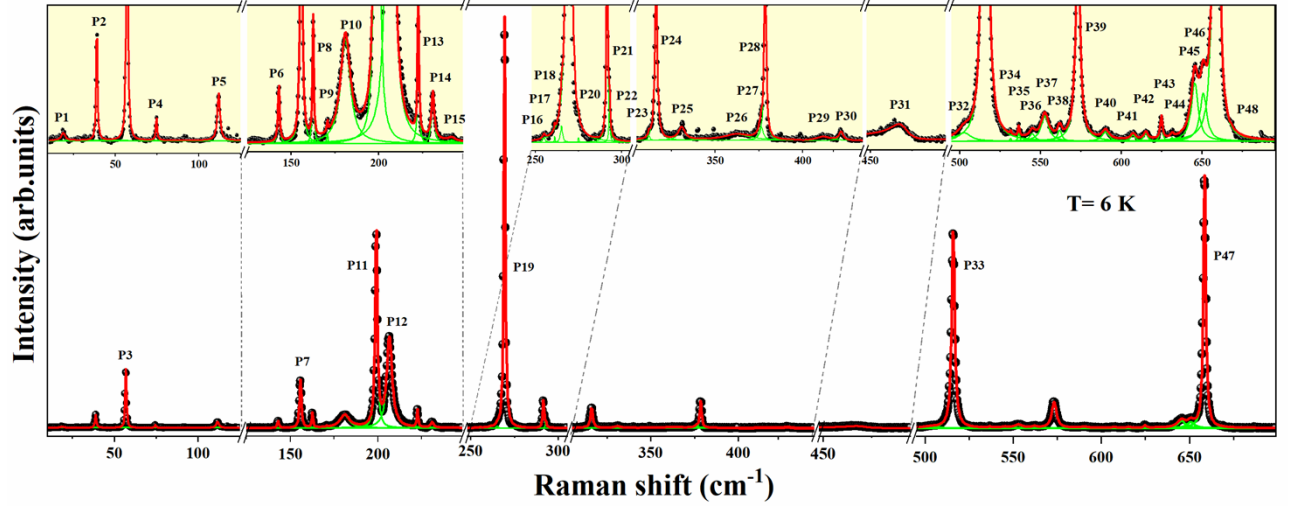
Figure S2. Fitted Raman spectrum of the single crystal of AgCrP$_2$S$_6$ in the spectral range of 15-700 cm^{-1} recorded at 6 K. The observed phonon modes are labelled as P1-P48. Solid thin line (green line) indicates the individual fit of the phonon modes and solid (red line) indicate the total fit of the Raman spectra.
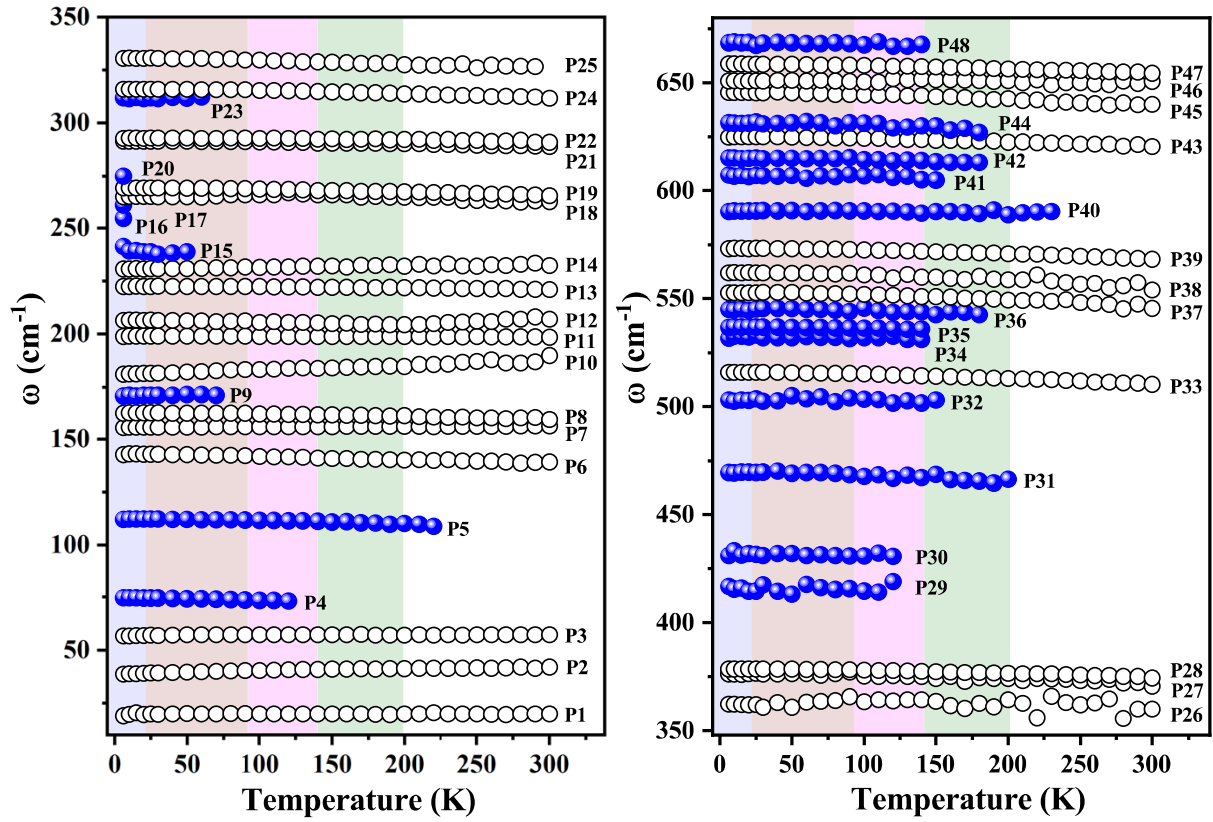
Figure S3. Temperature dependence frequency shift of all the observe phonon modes from P1-P48. Blue solid spheres represent the disappeared modes. Hollow circles represent phonon modes which survives at all temperatures. Blue, brown, pink, and green shaded regions show the temperature range of 0-20 K, 20-90 K, 90-140 K, and 140-200 K, respectively, which shows the regions of anomalies reflecting multiple transitions.
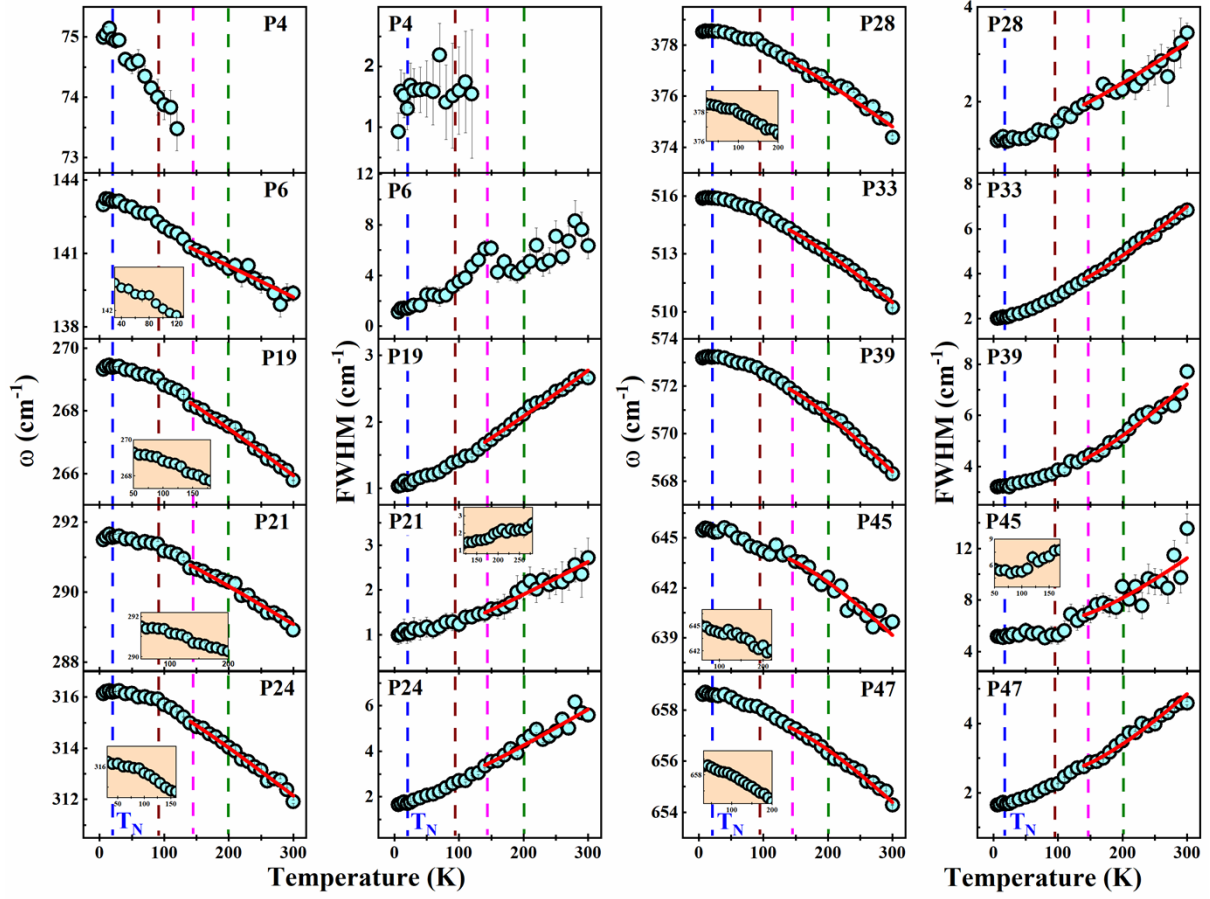
Figure S4. Temperature evolution of mode frequency and linewidth (FWHM) of phonon modes P4, P6, P19, P21, P24, P28, P33, P39, P45 and P47. The solid red line represents a three-phonon fitting in the temperature range of 140 to 300 K, whereas the dashed blue line indicates the antiferromagnetic transition at $T_N \sim 20$ K. The dashed brown, pink, and green lines reflect temperature anomalies at ~ 90 K, ~ 140 K, and ~ 200 K, respectively. Inset shows the magnified image of corresponding anomalies in frequency and FWHM.
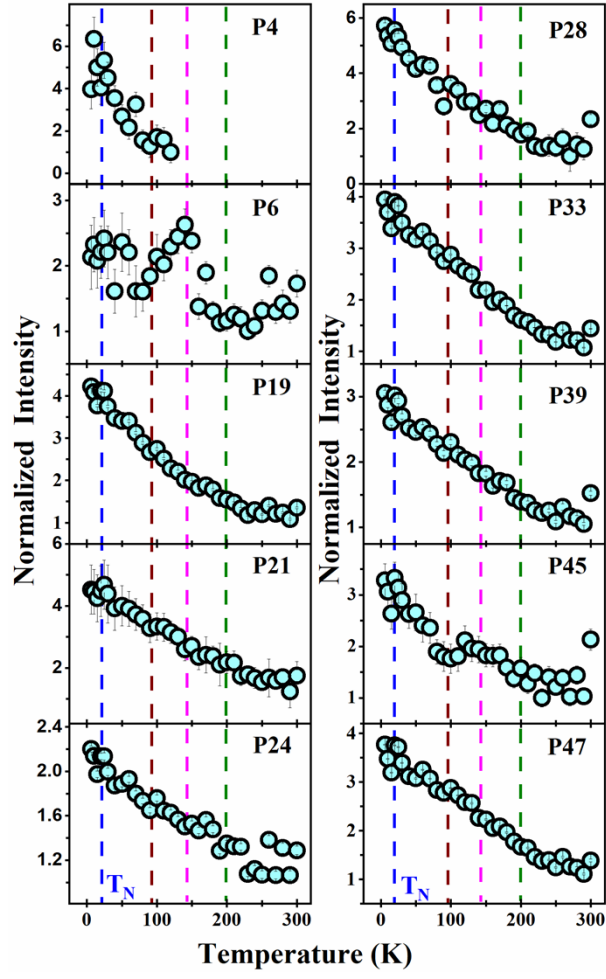
Figure S5. Shows temperature dependence of normalised intensity of modes P4, P6, P19, P21, P24, P28, P33, P39, P45 and P47.
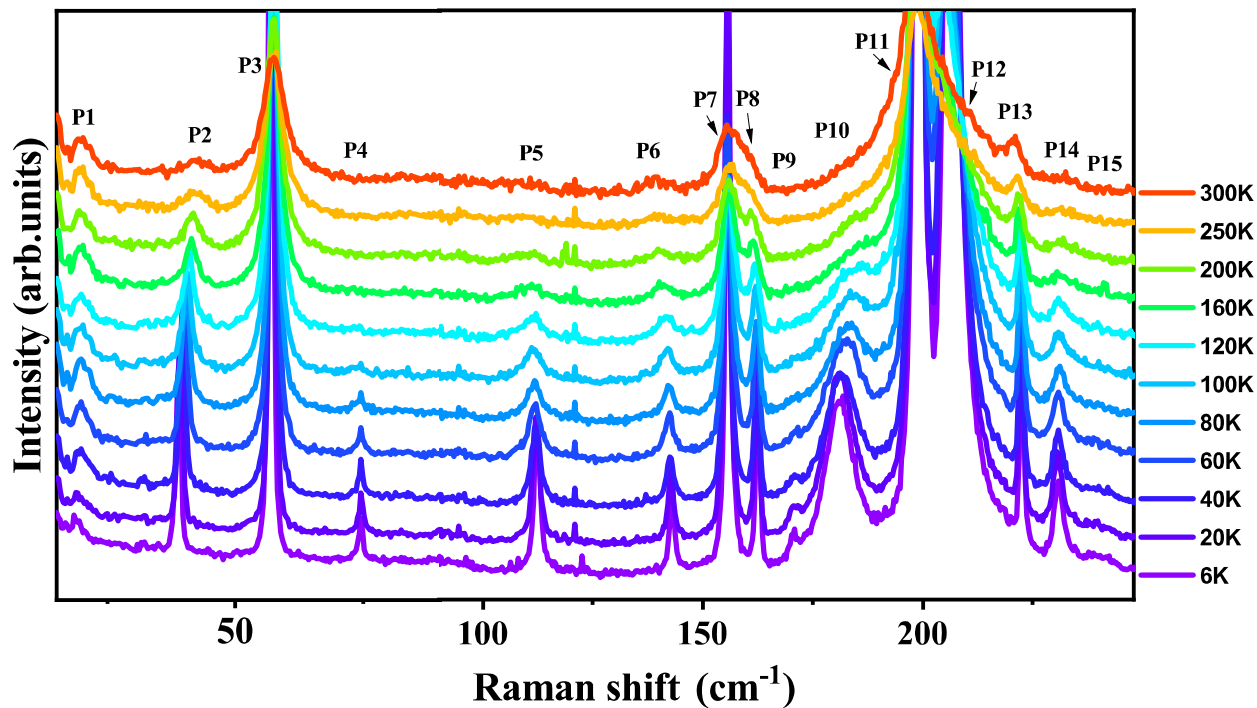
Figure S6. Shows Temperature evolution of the Raman spectrum of AgCrP$_2$S$_6$ in the frequency range of 15-250 cm^{-1}. Mode P4, P5, P9, and P15 disappeared at higher temperature.
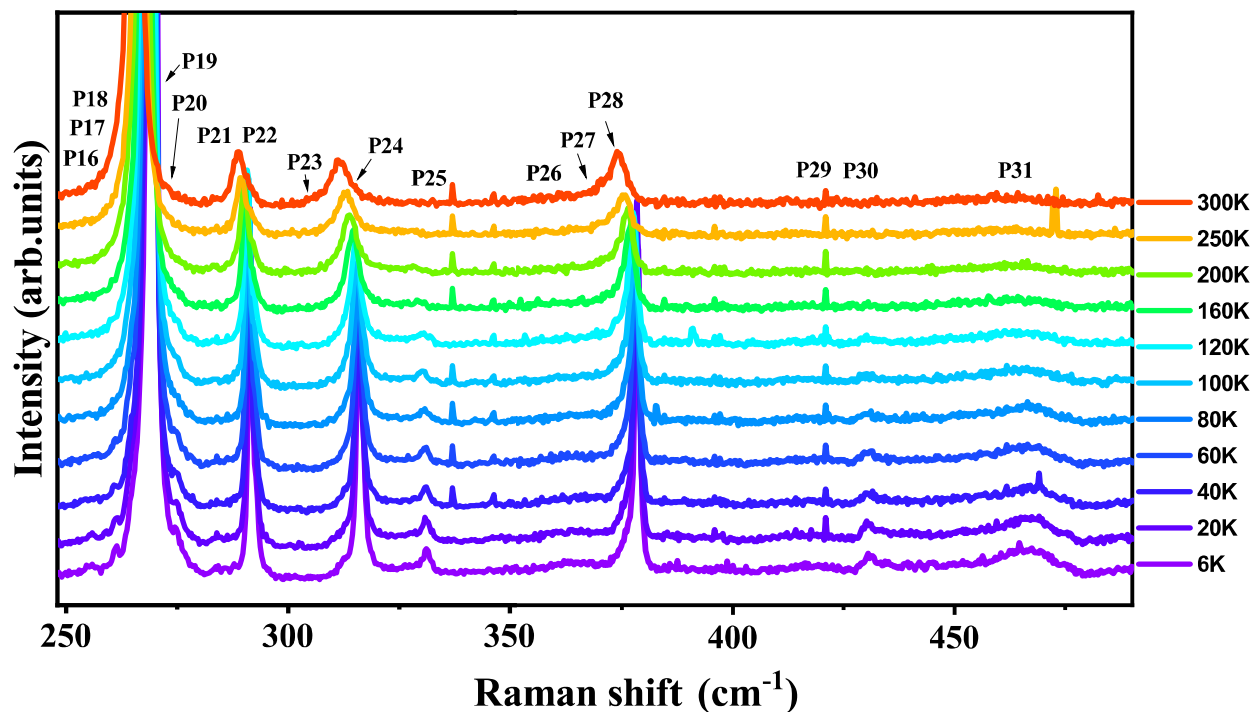

Figure S7. Shows Temperature evolution of the Raman spectrum of AgCrP$_2$S$_6$ in the frequency range of 250-490 cm^{-1}. Mode P16, P17, P20, P23, P25, P29, P30, and 31 disappeared at higher temperature.
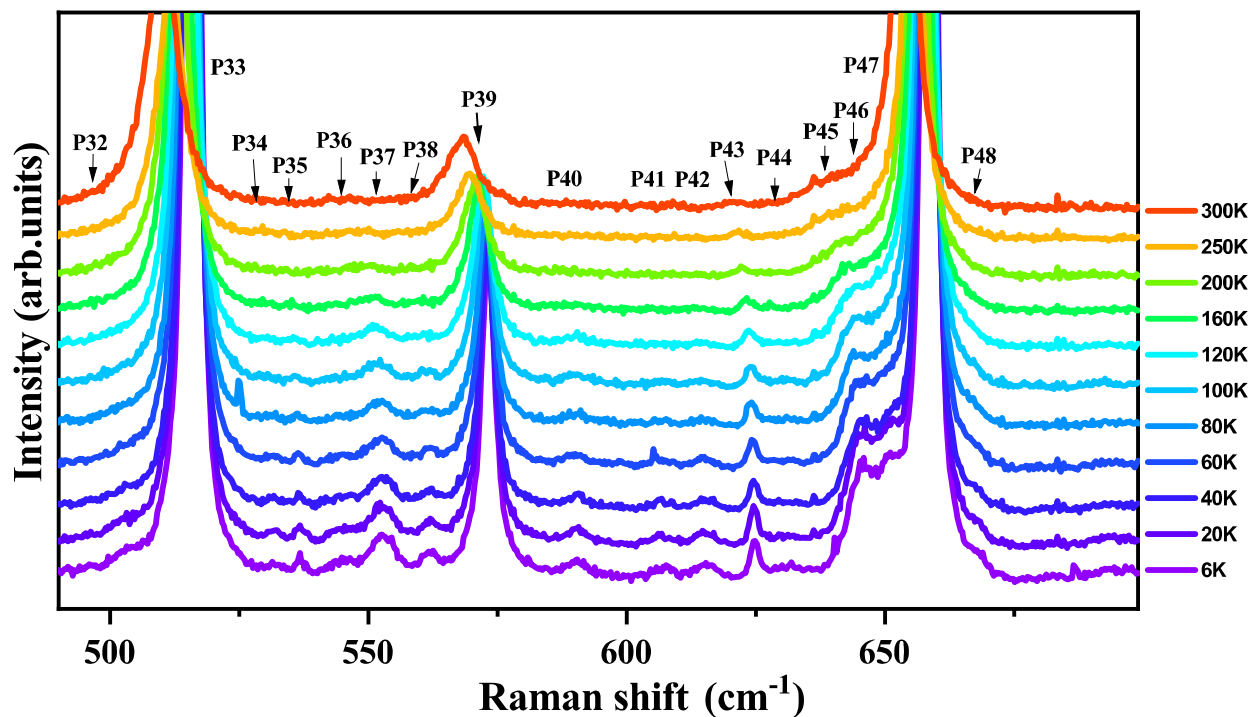
Figure S8. Shows Temperature evolution of the Raman spectrum of $AgCrP_2S_6$ in the frequency range of 490-700 cm^{-1}. Mode P32, P34, P35, P36, P40, P41, P42, P44, and P48 disappeared at higher temperature.

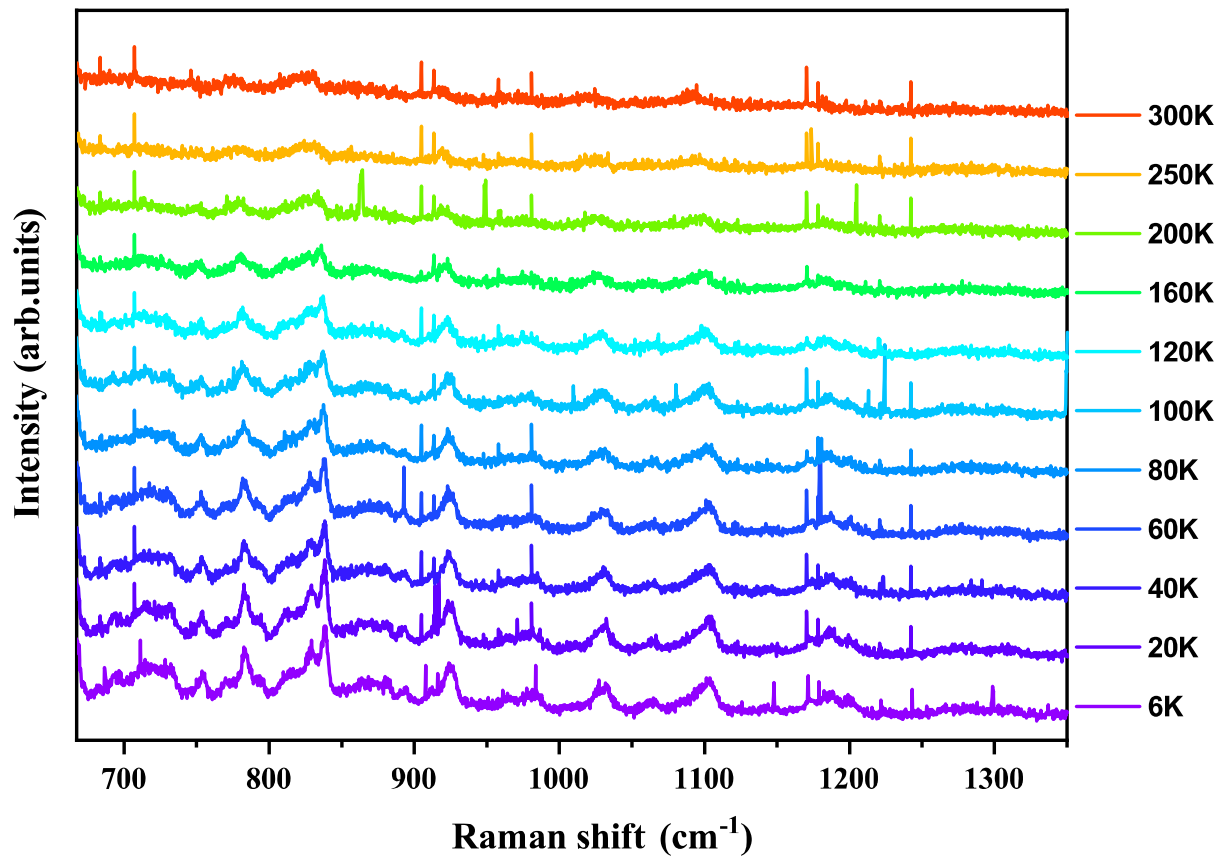**Figure S9.** Temperature evolution of higher order modes in the frequency range of 670 cm^{-1} to 1350 cm^{-1}.

Figure S10. Polarization-dependent intensity of the phonon modes P2, P3, P10, P12, and P14 measured at temperatures of 6 K, 60 K, 120 K, and 170 K, respectively; with varying incident light polarization. The solid red line at the bottom indicates the direction of the scattered light polarization.

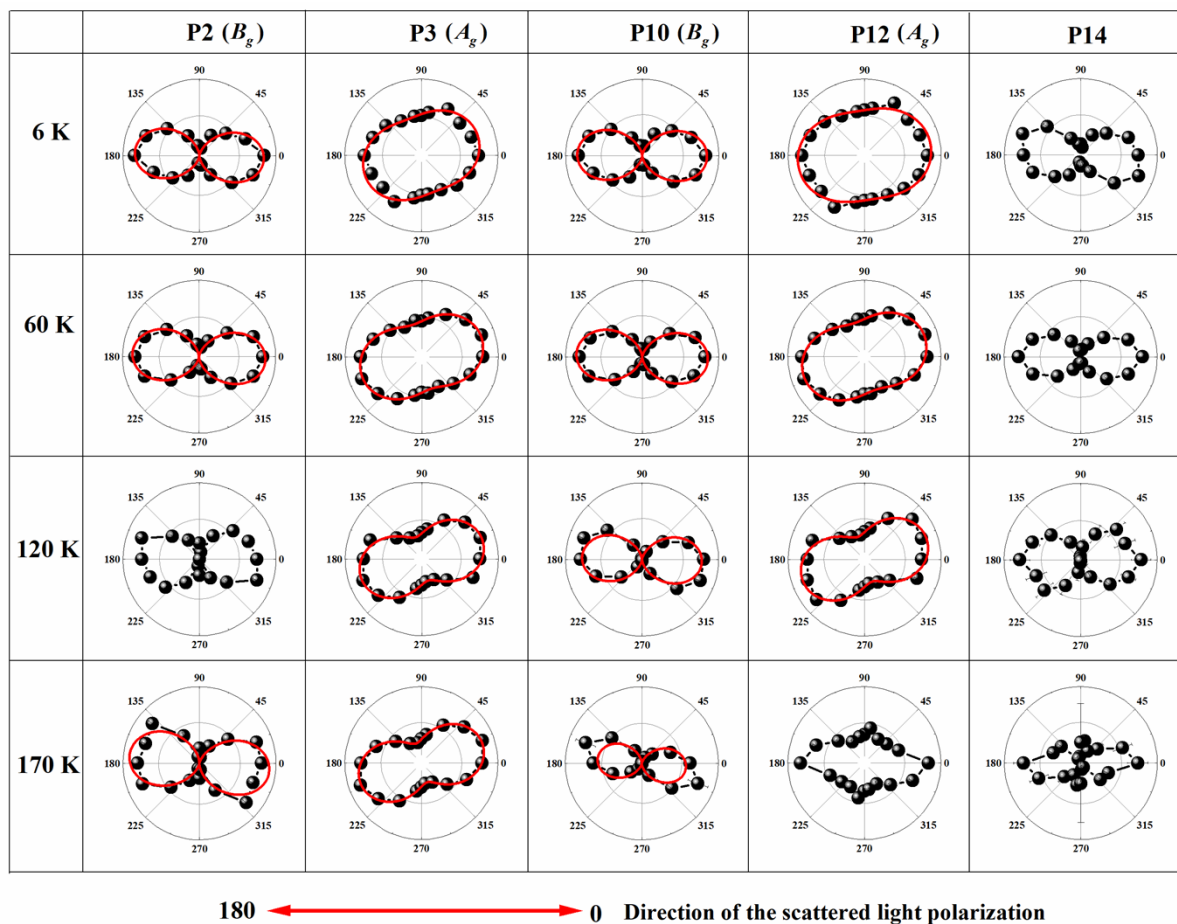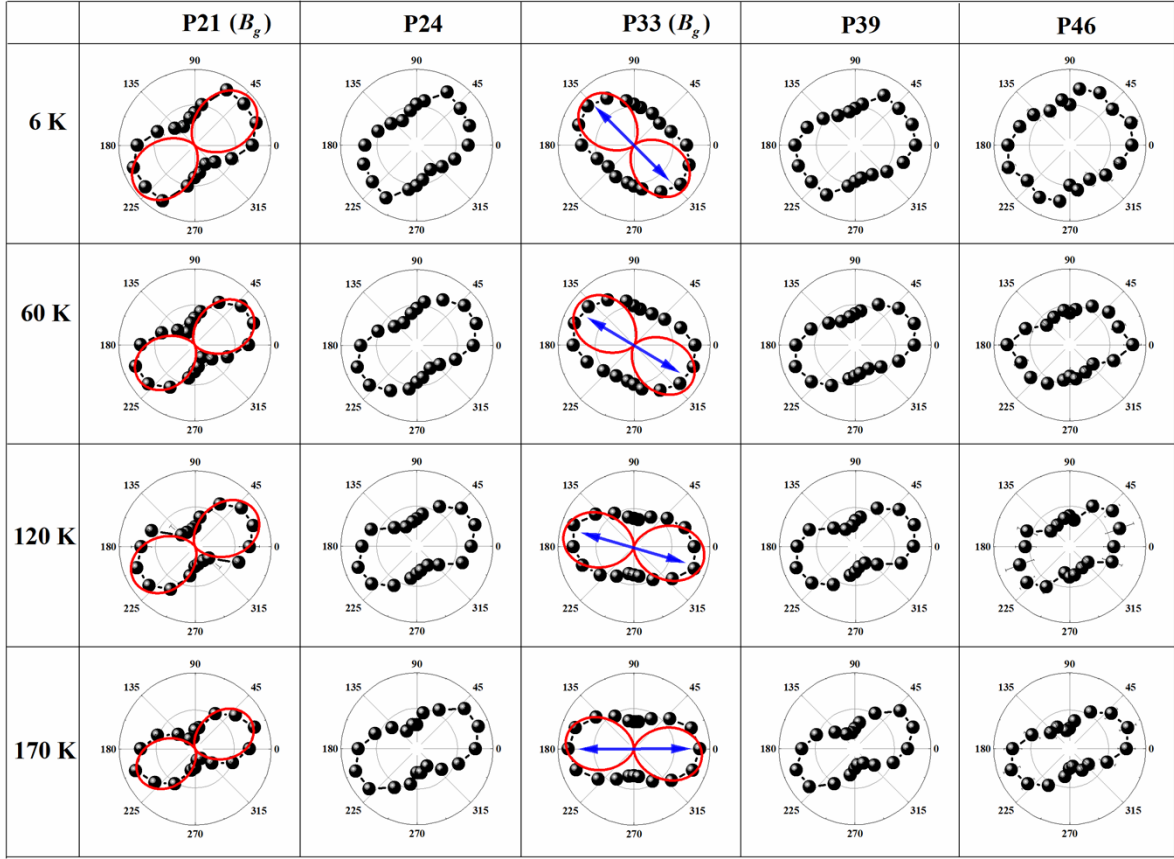**Figure S11.** Polarization-dependent intensity of the phonon modes P21, P24, P33, P39, and P46 measured at temperatures of 6 K, 60 K, 120 K, and 170 K, respectively; with varying incident light polarization. A blue arrow represents the rotation of the axis, showing the maxima as a function of temperature. The solid red line at the bottom indicates the direction of the scattered light polarization.
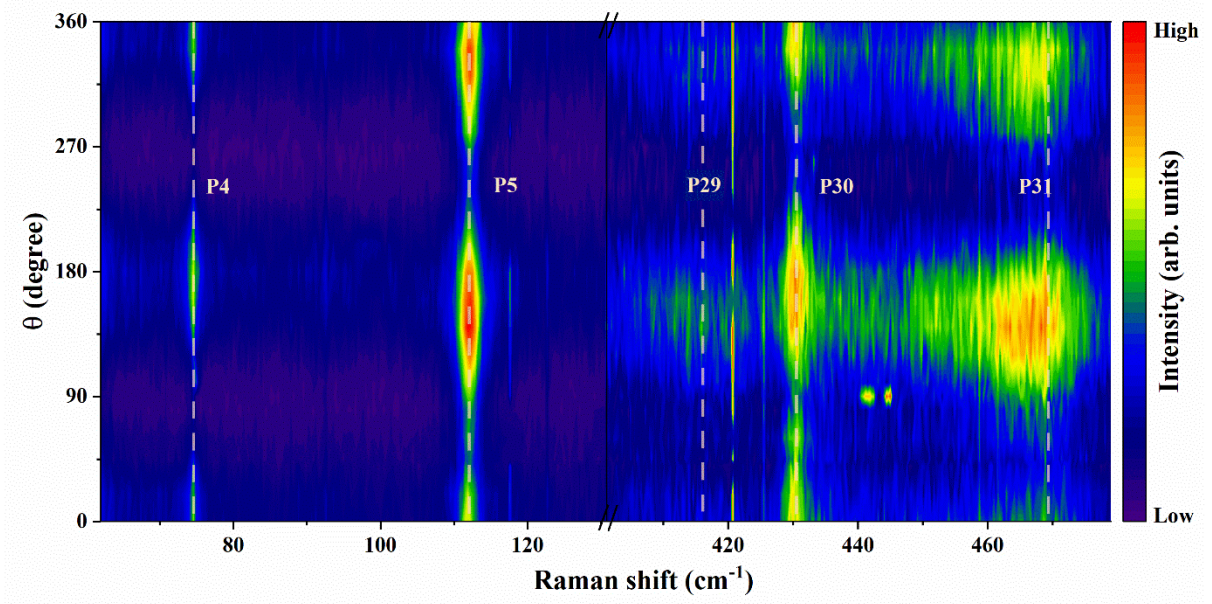
Figure S12. 2D colour contour map of polarization-dependent intensity of the phonon modes P4, P5, P29, P30, and P31 measured at 6 K.
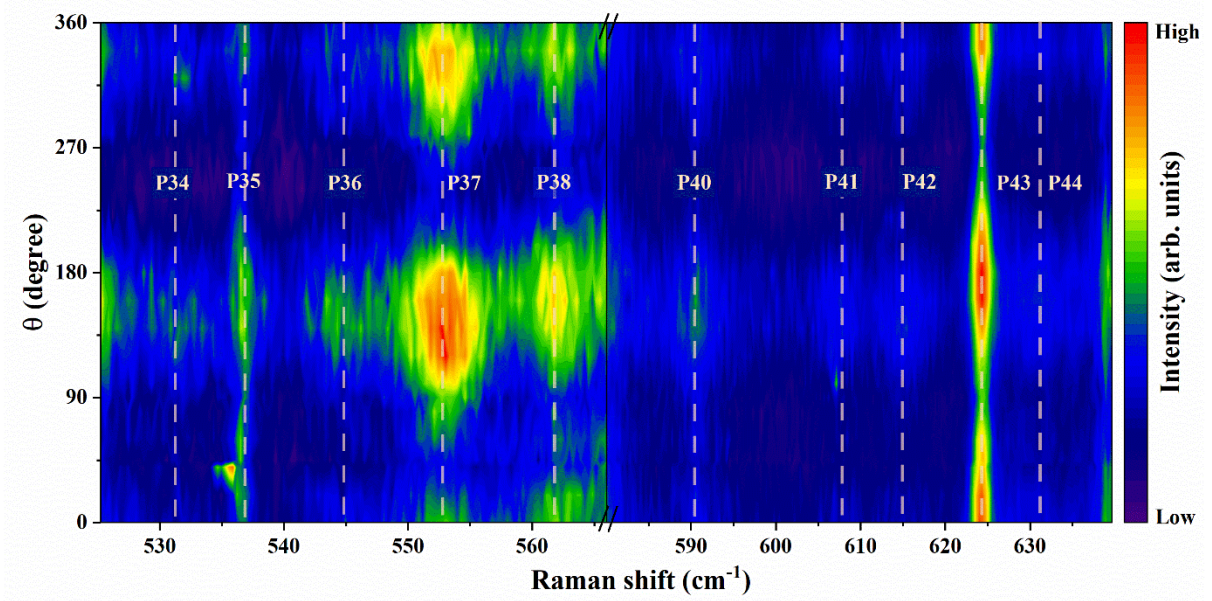
Figure S13. 2D colour contour map of polarization-dependent intensity of the phonon modes P34, P35, P36, P37, P38, P40, P41, P42, P43 and P44 measured at 6 K.
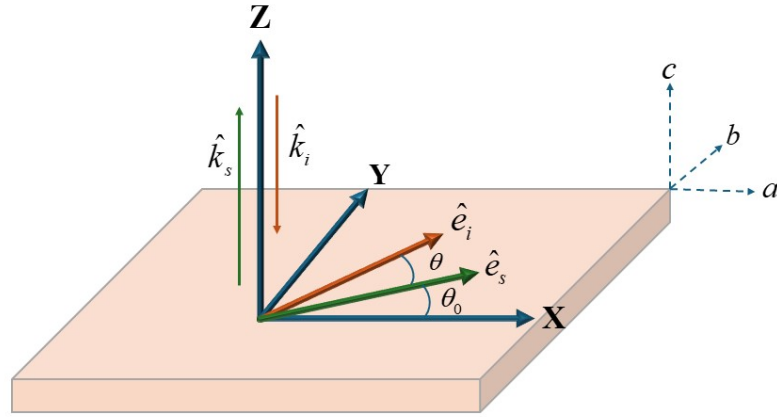
Figure S14. Schematic showing plane projection of the polarization direction of the incident ($\hat{e}_i$) and scattered light ($\hat{e}_s$) making angle $\theta + \theta_0$ and θ with X-axis, respectively. $\hat{k}_i$ and $\hat{k}_s$ represents the direction of incident and scattered beam.
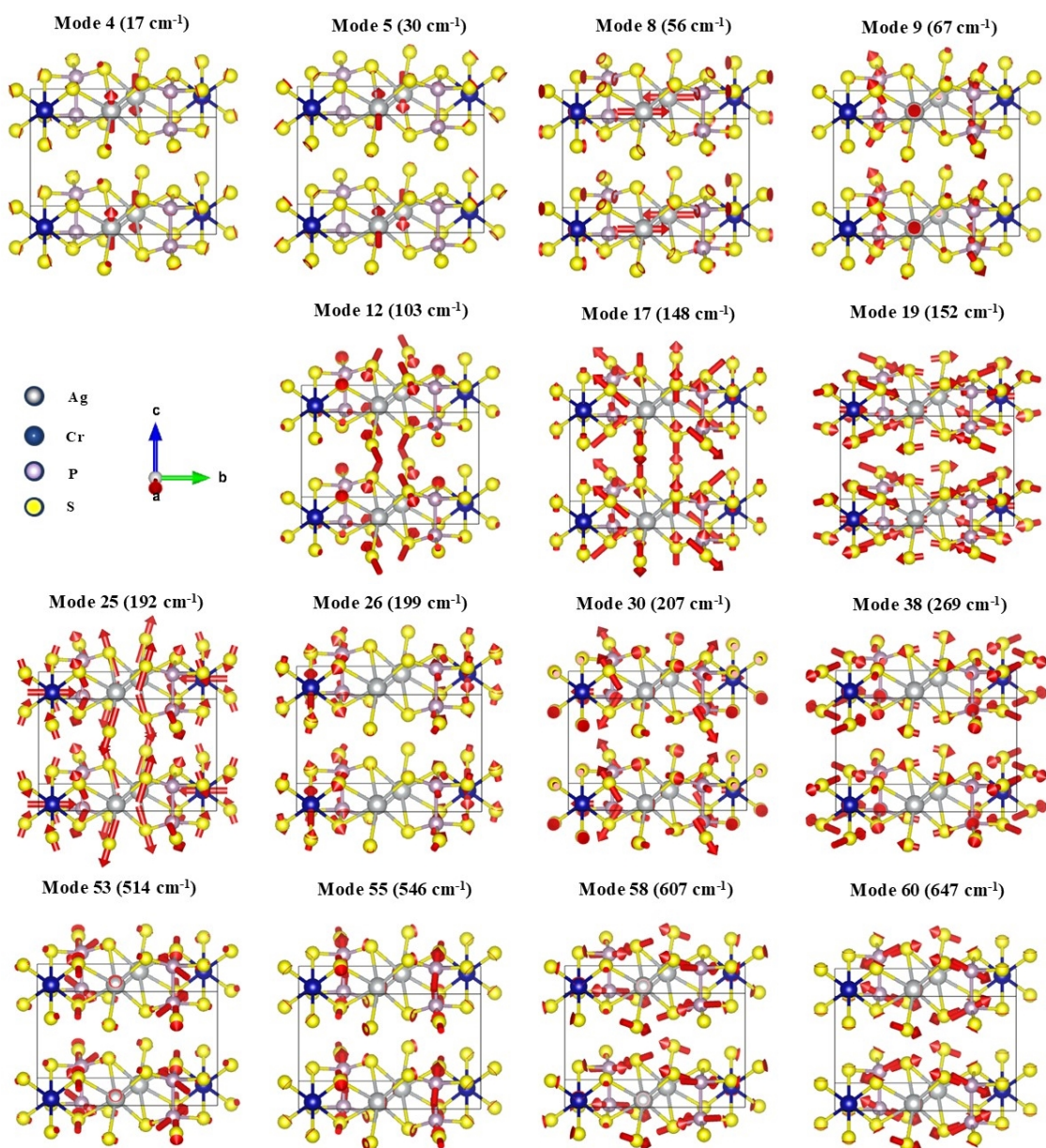
Figure S15. Mode visualization of some of the Raman active modes at Γ- point. Grey, blue, violet, and yellow spheres represent Ag, Cr, P, and S atoms, respectively. Red arrows on the atoms represent the direction of motion of the atoms and the size of the arrows represent the relative magnitude of vibration.
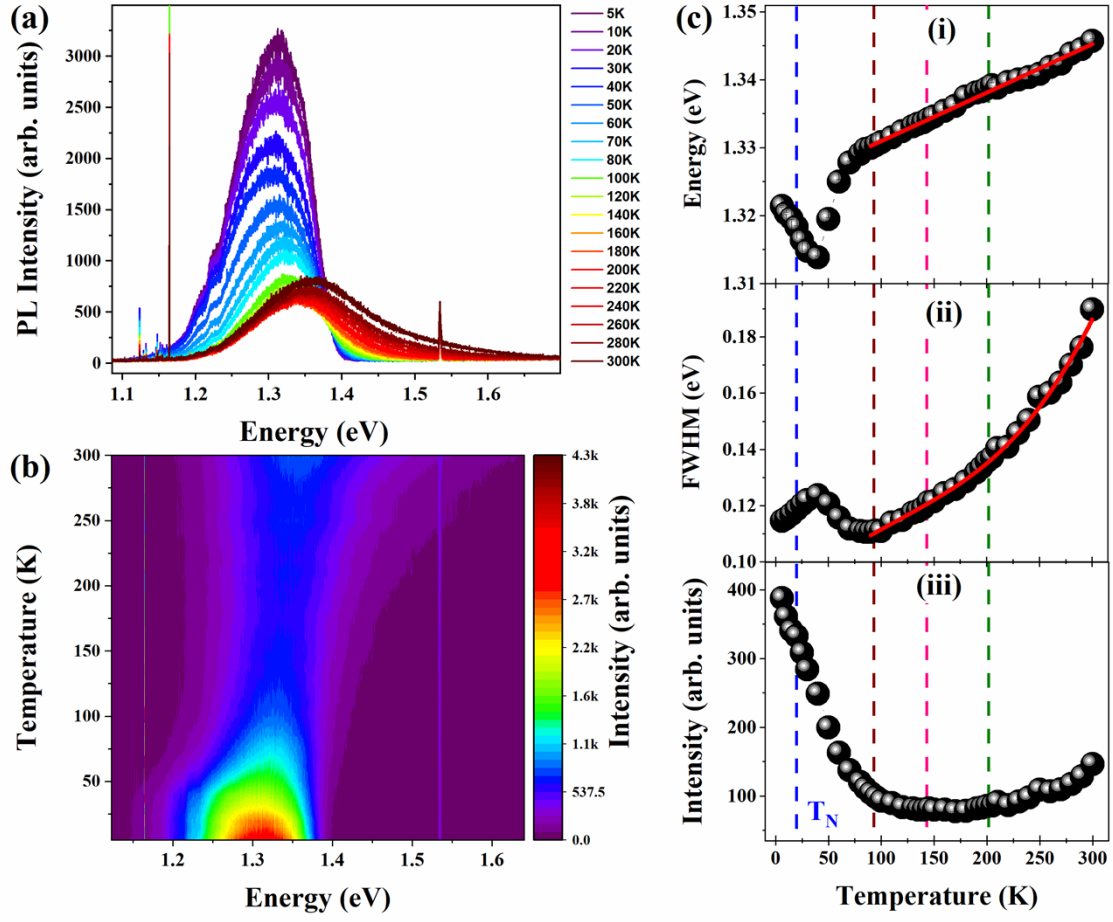
Figure S16. (a) Shows temperature evolution of PL. **(b)** Shows a colour contour plot of PL intensity in temperature-energy plane. **(c-i)** Temperature dependence of energy. **(c-ii)** Temperature dependence of FWHM. The red line shows the fitted curve as described in the text. **(c-iii)** Temperature dependence of PL intensity. The dashed blue line indicates the antiferromagnetic transition at $T_N \sim 20$ K. The dashed brown, pink, and green lines reflect temperature anomalies at ~ 90 K, ~ 140 K, and ~ 200 K, respectively.

Tables:

Table S1. List of the experimentally observed modes with their frequencies at 6 K and 300 K. The calculated phonon frequencies on the basis of first-principles calculations are denoted by ω_{DFT}. Units are in cm^{-1}.

Modes	ω (6 K)	ω (300 K)	Symmetry assignment	ω_{DFT}
P1	19.0 ± 0.10	19.9 ± 0.09	B_g	17
P2	38.8 ± 0.03	42.2 ± 0.18	B_g	30
P3	56.9 ± 0.01	57.5 ± 0.02	A_g	56
P4	74.9 ± 0.09	-	B_g	67
P5	112.3 ± 0.03	-	A_g	103
P6	142.9 ± 0.11	139.4 ± 0.34	B_g	148
P7	155.7 ± 0.01	156.4 ± 0.13	A_g	152
P8	162.5 ± 0.04	159.5 ± 0.21	B_g	156
P9	170.7 ± 0.41	-	A_g	169
P10	181.0 ± 0.15	189.9 ± 0.65	B_g , A_g	178, 192
P11	199.0 ± 0.00	198.6 ± 0.05	B_g	199
P12	206.5 ± 0.01	207.1 ± 0.43	A_g	207
P13	222.5 ± 0.04	221.1 ± 0.11	B_g	213
P14	230.9 ± 0.18	232.6 ± 0.45	-	-
P15	241.7 ± 4.05	-	-	-
P16	254.9 ± 3.81	-	-	-
P17	261.2 ± 0.88	-	-	-
P18	265.1 ± 0.85	263.0 ± 0.26	B_g	266
P19	269.3 ± 0.00	265.8 ± 0.01	A_g	269
P20	274.9 ± 0.72	-	A_g , B_g	278, 279
P21	291.4 ± 0.06	288.9 ± 0.17	B_g	293
P22	292.8 ± 0.36	291.1 ± 0.78	-	-
P23	312.1 ± 0.26	-	-	-
P24	316.1 ± 0.00	311.9 ± 0.06	-	-
P25	330.7 ± 0.18	-	A_g	346
P26	362.2 ± 0.94	359.8 ± 1.82	-	-
P27	376.1 ± 0.18	370.6 ± 0.42	-	-
P28	378.5 ± 0.00	374.4 ± 0.07	-	-
P29	416.7 ± 0.49	-	B_g	407
P30	431.0 ± 0.11	-	-	-
P31	469.5 ± 0.33	-	A_g	465
P32	503.0 ± 0.91	-	A_g	486

P33	515.8 ± 0.00	510.2 ± 0.01	B_g	514
P34	531.6 ± 0.73	-	-	-
P35	536.6 ± 0.24	-	-	-
P36	545.0 ± 0.75	-	A_g	546
P37	552.7 ± 0.25	545.4 ± 0.89	-	-
P38	561.9 ± 0.41	554.0 ± 1.78	-	-
P39	573.1 ± 0.02	568.3 ± 0.06	-	-
P40	590.3 ± 0.59	-	-	-
P41	607.2 ± 0.78	-	B_g	607
P42	615.2 ± 0.56	-	-	-
P43	624.8 ± 0.13	620.4 ± 0.41	-	-
P44	631.5 ± 0.93	-	-	-
P45	645.4 ± 0.14	639.9 ± 0.41	-	-
P46	650.7 ± 0.16	650.5 ± 0.44	-	-
P47	658.6 ± 0.00	654.3 ± 0.02	A_g	647
P48	668.5 ± 4.19	-	-	-

Table S2. Frequencies and symmetry labels of all 60 modes based on first-principles calculations of phonon frequencies at Γ - point for AgCrP$_2$S$_6$.

Mode No.	Frequency	Symmetry	Mode No.	Frequency	Symmetry
1	0	B_u	31	210	B_u
2	0	A_u	32	213	B_g
3	0	B_u	33	223	B_u
4	17	B_g	34	227	A_u
5	30	B_g	35	245	A_u
6	37	B_u	36	250	B_u
7	43	B_u	37	266	B_g
8	56	A_g	38	269	A_g
9	67	B_g	39	278	A_g
10	78	A_u	40	279	B_g
11	92	B_g	41	282	B_u
12	103	A_g	42	293	B_g
13	111	B_u	43	295	A_u
14	113	A_u	44	317	B_u
15	125	B_u	45	346	A_u
16	135	B_g	46	346	A_g
17	148	B_g	47	399	B_u

18	150	B_u		48	407	B_g
19	152	A_g		49	427	A_u
20	156	B_g		50	465	A_g
21	169	A_g		51	486	A_g
22	174	A_u		52	487	A_u
23	178	B_g		53	514	B_g
24	184	A_u		54	517	B_u
25	192	A_g		55	546	A_g
26	199	B_g		56	550	A_u
27	201	A_g		57	606	B_u
28	201	B_u		58	607	B_g
29	206	A_u		59	620	A_u
30	207	A_g		60	647	A_g

Table S3. List of fitting parameters for modes shown in Fig. 4 and Fig. S2 using three-phonon anharmonic model in the temperature range 140 K to 300 K. All units are in cm^{-1}.

Mode	ω_0	A	Γ_0	C
P2	40.3 ± 0.09	0.09 ± 0.01	-	-
P6	143.1 ± 0.16	-0.67 ± 0.04	-	-
P8	163.7 ± 0.16	-0.74 ± 0.05	-	-
P10	180.0 ± 0.47	1.62 ± 0.15	-	-
P13	223.2 ± 0.10	-0.48 ± 0.04	0.06 ± 0.28	0.86 ± 0.11
P19	270.8 ± 0.09	-1.53 ± 0.04	0.52 ± 0.05	0.71 ± 0.02
P21	292.7 ± 0.09	-1.22 ± 0.05	0.22 ± 0.12	0.81 ± 0.06
P24	318.5 ± 0.11	-2.31 ± 0.06	0.49 ± 0.26	1.95 ± 0.14
P28	380.8 ± 0.20	-2.56 ± 0.13	0.21 ± 0.19	1.29 ± 0.12
P33	520.8 ± 0.15	-5.73 ± 0.11	-1.92 ± 0.14	4.94 ± 0.10
P39	578.8 ± 0.16	-6.25 ± 0.12	-1.61 ± 0.33	5.31 ± 0.25
P45	654.5 ± 0.97	-10.11 ± 0.79	-3.67 ± 1.80	9.79 ± 1.45
P47	664.4 ± 0.21	-6.64 ± 0.18	-2.23 ± 0.24	4.69 ± 0.19

References:

[1]   R. Loudon, The Raman effect in crystals, Adv. Phys. **13**, 423 (1964).

[2]   J. Kim, J.-U. Lee, and H. Cheong, Polarized Raman spectroscopy for studying two-dimensional materials, J. Phys.: Condens. Matter **32**, 343001 (2020).

[3]   V. Funk, K. Wagner, E. Wietek, J. D. Ziegler, J. Förste, J. Lindlau, M. Förg, K. Watanabe, T. Taniguchi, and A. Chernikov, Spectral asymmetry of phonon sideband luminescence in monolayer and bilayer WSe_2, Phys. Rev. Research **3**, L042019 (2021).

[4]   A. Boziki, M. I. Dar, G. Jacopin, M. Gratzel, and U. Rothlisberger, Molecular origin of the asymmetric photoluminescence spectra of $CsPbBr_3$ at low temperature, J. Phys. Chem. Lett. **12**, 2699 (2021).

[5]   J. Diouri, J. P. Lascaray, and M. E. Amrani, Effect of the magnetic order on the optical-absorption edge in $Cd_{1-x}Mn_xTe$, Phys. Rev. B **31**, 7995 (1985).

[6]   Y. P. Varshni, Temperature dependence of the energy gap in semiconductors, Physica **34**, 149 (1967).

[7]   R. Pässler, Basic model relations for temperature dependencies of fundamental energy gaps in semiconductors Phys. Status Solidi B **200**, 155 (1997).

[8]   P. Lautenschlager, M. Garriga, S. Logothetidis, and M. Cardona, Interband critical points of GaAs and their temperature dependence, Phys. Rev. B **35**, 9174 (1987).

[9]   C. Yu, Z. Chen, J. J Wang, W. Pfenninger, N. Vockic, J. T. Kenney, and K. Shum, Temperature dependence of the band gap of perovskite semiconductor compound $CsSnI_3$, J. Appl. Phys. **110**, 063526 (2011).

[10]   S. Wang, J. Ma, W. Li, J. Wang, H. Wang, H. Shen, J. Li, J. Wang, H. Luo, and D. Li, Temperature-dependent band gap in two-dimensional perovskites: Thermal expansion interaction and electron–phonon interaction, J. Phys. Chem. Lett. **10**, 2546 (2019).

[11]   S. Rudin, T. Reinecke, and B. Segall, Temperature-dependent exciton linewidths in semiconductors, Phys. Rev. B **42**, 11218 (1990).

[12]   M. Leroux, N. Grandjean, B. Beaumont, G. Nataf, F. Semond, J. Massies, and P. Gibart, Temperature quenching of photoluminescence intensities in undoped and doped GaN, J. Appl. Phys. **86**, 3721 (1999).